Journal of Materials Chemistry A

Accepted Manuscript

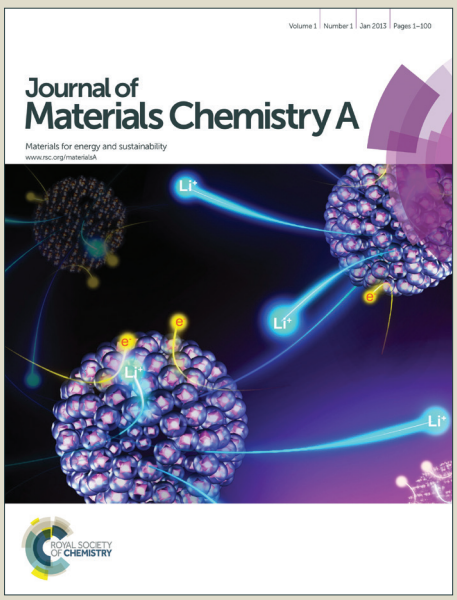

ROYAL SOCIETY OF CHEMISTRY

www.rsc.org/materialsA

Surface and Bulk Study of Strontium-Rich Chromium Ferrite Oxide as a Robust Solid Oxide Fuel Cell Cathode

*Min Chen, Scott Paulson, Wang Hay Kan, Venkataraman Thangadurai and Viola Birss**

Department of Chemistry, University of Calgary, Calgary, AB T2N 1N4, Canada

**Corresponding Author. Email: birss@ucalgary.ca*

ABSTRACT:

A novel Co-free cathode, $La_{0.3}Sr_{0.7}Fe_{0.7}Cr_{0.3}O_{3-\delta}$ (LSFCr-3), exhibiting the desired combination of high electrical conductivity, physical and chemical stability, and electrocatalytic activity, was systematically investigated for SOFC applications. Its excellent performance is attributed primarily to the presence of Cr, which was found to be predominantly in the 3+ and 4+ oxidation states in the LSFCr-3 bulk, thus likely maintaining a 6-fold coordination with oxygen anions. This, in turn, causes disorder in the oxygen vacancy sub-lattice, stabilized by the Fe ion-oxygen tetrahedra. However, on the surface of the LSFCr-3 oxide, Cr is primary in the +6 state, together with some Cr^{3+}/Cr^{4+}, even at 700 °C. Cr^{6+} can only be tetrahedrally coordinated by oxygen anions, resulting in a large concentration of oxygen vacancies on the LSFCr-3 surface, with a surface exchange coefficient and oxygen ionic conductivity of ca. 10^{-5} cm•s^{-1} and ca. 10^{-2} S•cm^{-1}, respectively, at 700-800 °C. The use of LSFC-3 as the cathode in a Ni-$Ce_{0.8}Sm_{0.2}O_{2-\delta}$ (SDC) anode-supported single solid oxide fuel cell in 3%H_2O-H_2/air gave a maximum power density of 0.81 W•cm^2 at 750 °C, which is superior to similar cells in which $La_{0.6}Sr_{0.4}Fe_{0.8}Co_{0.2}O_{3-\delta}$, a previously well studied material, was used as the cathode.

KEYWORDS: Solid oxide fuel cell; Cathode; Mixed conducting oxides; *In-situ* X-ray diffraction; *In-situ* X-ray photoelectron spectroscopy; Oxygen reduction reaction

1. Introduction

Solid oxide fuel cells (SOFCs) are high efficiency energy conversion devices that also have a number of environmental advantages, including low to zero emission of pollutants (SO_x, NO_x and particulates) and the generation (capture) of a clean and nearly pure stream of CO_2 (no N_2) ready for storage. In order to make SOFC technology more competitive with mature power generation technologies based on fossil fuel combustion, it is necessary to further improve SOFC durability under practical operating conditions. This can only be achieved by employing sufficiently stable electrolyte and electrode materials. The durability of these materials is dictated primarily by their physical stability, associated with their thermal expansion compatibility, as well as their chemical stability, related to phase stability and interfacial reactions that may occur under polarization.

As is generally recognized, the cathode is normally the main cause of polarization losses in SOFCs, consistent with their dramatic loss in activity when operating temperatures are lowered. Therefore, highly active cathode materials are required to decrease the resistance of the oxygen reduction reaction (ORR) at lower temperatures. To date, most high performing cathodes are based on Co-containing perovskite oxides and related structures, such as $La_{1-x}Sr_xCo_yFe_{1-y}O_{3-\delta}$ [1, 2], $Ba_{1-x}Sr_xCo_yFe_{1-y}O_{3-\delta}$ [3, 4], $LnBaCo_2O_{5+\delta}$ [5] (Ln = rare earth elements, such as Pr, Sm, Gd, etc.) and $SrCo_{0.95}Sb_{0.05}O_{3-\delta}$ [6]. However, from the viewpoint of durability, their poor structural stability and relatively large thermal expansion coefficients (TECs) lead to limitations for practical application in SOFCs, found to be associated with the valence state and spin state transitions of the Co ions present in the B site of all of these promising materials. Furthermore, the high price of Co is a problem for SOFC commercialization.

Thus, there is significant interest in developing low-Co content or Co-free SOFC cathodes [7-10]. For example, Fe-based perovskite oxides have attracted considerable attention because of their stability in oxidizing environments and their good electrocatalytic activity towards the ORR. The

$La_{0.6}Sr_{0.4}Fe_{0.8}Co_{0.2}O_{3-\delta}$ (LSCF) cathode, a typical Fe-based perovskite oxide but having a relatively low Co content, has been widely used in SOFC stacks over the past few years [11,12].

Another challenge is that, depending on the cathode kinetics and the magnitude of the current passed, the local oxygen partial pressure (pO_2) at the triple phase boundary (TPB) can be lower than in the gas phase, thus leading to partially reducing conditions [13]. This oxygen starvation problem becomes worse under high cathodic polarization conditions (i.e., high oxygen utilization). However, the widely used LSCF cathode material is not stable under reducing conditions [14], resulting in degradation of the cell performance or even complete failure of the cell. Accordingly, the development of new cathodes that are stable under both oxidizing and reducing atmospheres is a meritorious objective.

Extensive work by Irvine et al. has shown that perovskite oxides containing high valence transition metals (Nb, Ti, Mo, V and Cr) in the B-site are stable over a wide range of pO_2, while low valence transition metals (Co, Ni, Cu and Zn) in the B-site usually bring about phase decomposition under reducing conditions [15]. Thus, to design a Fe-based perovskite cathode material with excellent stability under all of these conditions, one approach is to lightly substitute for Fe in the B-site with a higher valence transition metal. In terms of this strategy, several new compositions have been investigated as potential cathodes for SOFCs [16-20], as listed in Table S1 (See Supporting Information). As is generally recognized, it is challenging to achieve the necessary combination of good electrical conductivity, chemical stability, and electrocatalytic activity characteristics.

In our previous work, a novel Sr-rich chromium ferrite, having a composition of $La_{0.3}Sr_{0.7}Fe_{0.7}Cr_{0.3}O_{3-\delta}$ (LSFCr-3, composition (8) in Table S1, see Supporting Information), was investigated as an electrode material for symmetrical SOFCs [19]. Similar materials, e.g., $LaSr_2Fe_{3-y}Cr_yO_{8+\delta}$ oxides, targeted as membrane materials for the partial oxidation of natural gas and for use as SOFC anodes, have exhibited excellent ionic and electronic conductivity at oxygen partial pressures ranging from 0.5 to 10^{-22} atm [21, 22]. We also found that LSFC-3 is an active and robust SOFC cathode,

and its electrochemical performance and TEC compatibility with most electrolytes were both shown to be superior to what has been reported for the LSCF cathode. LSFCr-3 exhibited an electrical conductivity of 75-105 $S \bullet cm^{-1}$ at 600-800 °C in air, reaching the desired electrical conductivity values ($\geq$ 100 $S \bullet cm^{-1}$) for a cathode material for SOFC applications. In addition, LSFCr-3 was found to be structurally stable over many orders of magnitude of pO_2 change, from a pO_2 of 0.21 atm typical for a cathode to a pO_2 of 10^{-21} atm for use as an anode [19]. This excellent stability of LSFCr-3, even under fuel-rich conditions, is consistent with what is needed for LSFCr-3 to be a durable cathode at very high current densities (low cell voltages) or when crossover of fuel into the cathode compartment occurs due to leakage of the electrolyte or seals.

When designing the composition of the LSFCr-3 perovskite (ABO_3), the A-site La:Sr ratio and the B-site Fe:Cr ratio were tailored to achieve the best overall performance of the resulting cathode. Heavy A-site substitution of La by Sr (Sr-rich composition) was used to increase the electronic and ionic conductivity, resulting in a long triple-phase boundary (TPB) for the ORR. The Cr constituent in the 3+ and 4+ oxidation state, which has a strong preference for 6-fold coordination with oxygen anions [21], has been shown to induce disordering of the oxygen vacancies, which are otherwise stabilized (ordered) by the Fe cations. The addition of Cr has thus been demonstrated to improve the durability of the cathode material [19].

In the present study, the crystal structure of the LSFCr-3 perovskite and the oxidation state of the B-site cations (Fe and Cr) were determined *in-situ* in air from room temperature to 800°C. The electrical conductivity, oxygen ionic conductivity, bulk diffusion coefficient, and surface exchange coefficient were also systematically determined in relation to the use of LSFCr-3 as an oxygen reduction electrode. Further, the electrocatalytic activity of the LSFCr-3 material toward the ORR was studied and the rate determining step was identified. Importantly, we provide a first-time demonstration of the beneficial effects of Cr in a perovskite-based cathode, explained in terms of the oxidation state of Cr in both the surface and bulk regions of the LSFCr-3 perovskite.

2. Experimental

2.1 Synthesis

A glycine nitrate process was employed to prepare LSFCr-3 powder with a nominal composition of $La_{0.3}Sr_{0.7}Fe_{0.7}Cr_{0.3}O_{3-\delta}$ (actual composition is $La_{1/3}Sr_{2/3}Fe_{0.7}Cr_{0.3}O_{3-\delta}$). The details of the wet-chemical synthesis, calcination steps and grinding processes were reported in our previous study [19]. The resulting powders were divided into three portions for rigorous characterization, with one portion employed to determine the crystal structure and oxidation states of the B-site cations (Fe and Cr) in LSFCr-3 *in situ*. The second portion of the LSFCr-3 powder was used for the electrical conductivity measurements, while the third was employed for electrochemical testing, thus ensuring that the same material was being investigated in all cases.

2.2 Structural Characterization

The crystal structure of the LSFCr-3 samples was determined by room temperature powder X-ray diffraction (PXRD) measurements using a Bruker D8 Advance X-ray diffractometer (Cu K_α, 40 kV, 40 mA). Typically, measurements were performed from 2θ = 10º to 80 º at a count rate of 15 s per each 0.02 º step at ambient conditions. Rietveld refinements on the PXRD patterns were carried out using the GSAS package with the EXPGUS interface.

The crystal structure evolution of the LSFCr-3 oxides was tracked by *in-situ* PXRD measurements with a high temperature reactor chamber (Anton Paar XRK 900). Samples were heated to the target temperatures at a ramp rate of 6 °C/min and stabilized in air for 30 min prior to measurements. *In-situ* PXRD patterns were collected in the 2θ range of 10-80 ° at a count rate of 6 s per each 0.05 ° step. The cell parameters at each temperature were determined using MDI Jade 5.0 software.

The cation stoichiometry of the LSFCr-3 oxide was verified using Inductively Coupled Plasma Mass Spectrometry (ICP-MS, Agilent 7500a). 10 mg of the powder was dissolved into ca. 4 M HCl and then diluted with water until each element was determined to have a concentration lower than

300 ppm. The oxygen non-stoichiometry (δ) and the average oxidation state of the B-site cations (Fe and Cr) at room temperature were determined by iodometric titration. Approximately 0.1 g of the as-prepared powders was dissolved into ca.15 ml of 4 M HCl, following by mixing with 15 ml of 10 wt.% KI. As soon as the Fe and Cr cations were sufficiently reduced, the resulting solution was titrated with standardized 0.1 M $Na_2S_2O_3$ using a starch solution as the indicator under a N_2 atmosphere [16].

The variation in δ for the powder samples was determined as a function of temperature and pO_2 using thermogravimetric analysis (TGA) methods (Mettler Toledo Thermal Analysis, TGA/DSC1). In order to achieve thermodynamic equilibrium during heating (up to 900 °C) of the oxide powders in air, a relatively low ramp rate of 1 °C/min was used. To determine the effect of pO_2 on the δ values, TG measurements were carried out at 700, 750 and 800 °C. At each of these temperatures, the sample was initially equilibrated for 2 h in air and then, a mixture of N_2 and air was introduced to adjust the pO_2 values in the range of 0.04-0.21 atm. The oxygen non-stoichiometry (δ) of the LSFCr-3 material at various temperatures and pO_2 was then calculated using [16]:

$$\delta = \frac{M_0}{15.999}\left(1-\frac{m}{m_0}\right)+\delta_0 \qquad (1)$$

where m_0 is the starting weight and m is the final weight of the sample at various temperatures and pO_2 conditions during the TGA measurements, δ_0 is the oxygen non-stoichiometry at room temperature, M_0 is the molar mass of the samples at room temperature, and 15.999 is the atomic weight of oxygen atom.

In order to determine the oxidation state of Fe in the LSFCr-3 perovskite, ^{57}Fe Mössbauer spectroscopy analysis was performed with a conventional constant-acceleration spectrometer (MB-500) and using a ^{57}Co source in an Rh matrix at room temperature. The velocity scale was calibrated using an α-Fe foil. Mössbauer spectra of the samples were fitted to a Lorentzian line using the Fit ;o) Mössbauer fitting program. The parameters associated with each fitted peak, including the isomer shift and relative intensity, were then resolved.

For the *in-situ* (high temperature) X-ray photoelectron spectroscopy (XPS) and electrical conductivity measurements, the LSFCr-3 powders were uniaxially pressed into disks under a pressure of 100 MPa, followed by sintering at 1300°C for 4 hours in air. The density of the specimens was determined using the Archimedes method, giving a value of around 95%. XPS measurements were carried out *in-situ* using a Thermo Scientific ESCALAB 250Xi spectrometer with an in house high temperature stage. Measurements were conducted from room temperature to 700 °C. The working pressure in the XPS chamber at room temperature, 300 °C, 500 °C, 600 °C and 700 °C was 4×10^{-9} mbar, 1×10^{-8} mbar, 3×10^{-7} mbar, 5×10^{-7} mbar and 8×10^{-7} mbar, respectively. This increase in the working pressure with increasing temperature was caused primarily by outgassing of any hydrocarbons or moisture contained in the samples.

An incident monochromaticized X-ray beam (hν = 1486.7 eV) from the Al target was focused on a 400 μm area of the sample surface. Emitted photoelectrons were detected by a multichannel detector at a take-off angle of 90 ° relative to the sample surface. A step size of 1 eV was employed to carry out a survey scan in the binding energy range of 0-1200 eV. Detailed scans were recorded for the Sr3d, La3d, Fe2p, Cr2p, C1s and O1s regions, with a step size of 0.1 eV. All of the obtained binding energies (BEs) were calibrated, using the adventitious carbon (C1s) peak at 284.5 eV as a reference. The XPS peaks were analyzed (CasaXPS software) using a Shirley-type background and nonlinear least-squares fitting of the experimental data based on a mixed Gaussian/Lorentzian peak shape.

2.3 Electrical conductivity

To measure the electrical conductivity of the LSFCr-3 samples, the dense pellets were polished to form a flat sheet (21.7 mm in diameter and 1.08 mm in thickness) and were then painted with four contacts (probe) using Pt paste. All four probes (distance between the probes was 12 mm) were made of Pt beads, which were pressed onto the pre-painted contacts (Pt paste) on the pellets. The

electrical conductivity of the samples was determined at 700-800 °C in various pO_2 environments by using the standard dc Van der Pauw method with a constant current source (Agilent E3615A, 25 mA in this study) combined with a digital multimeter (Agilent 34420A). The pO_2 was adjusted using a gas mixture of O_2, air, N_2, CO, CO_2 and H_2, while the gas flows were controlled with Alicat mass flow controllers.

A solid zirconia electrolyte oxygen sensor (Ceramic Oxide Fabricators, $SIRO_2$ C700+) was integrated into the conductivity test fixture to monitor the pO_2 values. The electrical conductivity measurements were carried out by decreasing the pO_2 in isothermal runs. In order to ensure that the pO_2 over the sample changed immediately after varying the gas composition, the gas inlet was placed very close to the sample surface. It was found that the relaxation time after a change in pO_2 over a sample was dependent on the temperature and pO_2 range. The accepted criterion for having achieved equilibrium at a fixed pO_2 was a electrical conductivity change of less than 1% per hour.

Electrical conductivity relaxation (ECR) measurements were carried out in the high pO_2 range to determine the chemical diffusion coefficient (D_{chem}) and the oxygen surface exchange coefficient (k_{ex}) of the LSFCr-3 material in an environment typically experienced by SOFC cathodes. Initially, the sample was fully equilibrated in a pO_2 of 0.1 atm, after which a sudden change of pO_2 from 0.1 to 0.21 atm was achieved by changing the gas mixture. The time dependence of the conductivity was recorded until a new steady-state was reached. After each test, the sample was stabilized for 1 h before the conditions were altered.

2.4 Electrochemical characterization

The $La_{0.8}Sr_{0.2}Ga_{0.8}Mg_{0.2}O_{3-\delta}$ (LSGM, fuelcellmaterials.com) electrolyte powders were cold isostatic pressed into 20 mm pellets under a pressure of 100 MPa and pre-sintered at 1100 ^oC for 2 hours in air to ensure adequate strength. Next, a $La_{0.4}Ce_{0.6}O_{2-\delta}$ (LDC) buffer layer was coated onto both sides of the LSGM substrate using screen printing, followed by co-sintering at 1350^oC for 4

hours. The thickness of the resulting dense electrolyte support was ca. 1.1 mm and the diameter was 16 mm. The LSFCr-3 powders were then screen printed symmetrically (1.0 cm^2 area) onto both sides of the LSGM support and fired at 1100 ^oC for 2 hours. Au paste (C 5729, Heraeus Inc. Germany) was then painted on the LSFCr-3 layers on both sides of the pellet to serve as the current collectors.

The obtained 2-electrode half cells, containing symmetrical LSFCr-3 electrodes were used for electrochemical impedance spectroscopy (EIS) studies. To determine the LSFCr-3 performance in an anode-supported single cell, a YSZ/$Ce_{0.8}Sm_{0.2}O_{2-\delta}$ (SDC) bi-layer electrolyte membrane, supported by a Ni-SDC cermet, was selected. The details of fabrication of the anode-supported cell (coin) containing the LSFCr-3 cathode layer were given in our previous work [19, 20].

The cells were fixed in a FCSH-V3 cell holder (MaterialsMate, Italy) for the purpose of determining their electrochemical properties. For half cell testing, a single chamber mode was used, in which the pO_2 was varied between 0.04 and 1 atm using O_2/air-N_2 mixtures. For anode-supported single cell testing, a glass sealant (Type 613, Aremco Products, USA) was used to isolate the anode (wet (ca. 3%H_2O)-H_2) and cathode (air) gases.

The cell performance, including I-V (current density-voltage) and I-P (current density-power density) characteristics, was evaluated using a four-probe method at 750 ^oC. Impedance spectra of the half-cells (750 ^oC in air) were collected at the open circuit potential and under DC bias conditions using a RMS amplitude of 50 mV in the frequency range of 0.01 Hz to 60 kHz (Solartron 1287/1255 potentiostat /galvanostat/impedance analyzer). Using the ZView (version 3.1) software, the impedance data were then analyzed.

3. Results and Discussion

3.1. Crystal structure of LSFCr-3 perovskite

In our previous study [19], PXRD analysis of the LSFCr-3 oxide suggested that it was composed of a single perovskite phase containing no detectible impurities after firing at 1200 °C in air for 4 h. To

obtain more structural information, the crystal structural of the LSFCr-3 material was further analyzed by Rietveld refinement in this study, with the profiles shown in Fig. 1(a). It is seen that LSFCr-3 actually has a hexagonal structure *(R-3c)* with a = 5.4950(2) Å, c = 13.4369(9) Å, and a unit cell volume of 351.715 Å^3. The profile R-value (R_p), weighted-profile R-value (R_{wp}), and the Durban-Waston parameter of the refined structure parameters were 6.3%, 8.5% and 1.325, respectively, indicating that the refinement results are acceptable.

To serve as a cathode material for SOFCs, an electrode must be stable during heating, operation, and cool-down. Therefore, to track the phase evolution of LSFCr-3 with respect to temperature, *in-situ* high temperature PXRD measurements were carried out from room temperature to 900 °C. As shown in Fig. 1(b), the hexagonal structure was maintained at temperatures up to 900 °C, since no splitting was observed for the characteristic (110) and (024) peaks in the 2θ range of 31-34° and 45-48°, respectively. In addition, a shift of the (110) and (024) diffraction peaks toward lower angles is seen, suggesting an increase in the cell parameters with increasing temperature.

Fig. 1(c) displays the thermal expansion curves of the cell parameters (a, c and unit cell volume), resolved by refining the corresponding PXRD patterns at various temperatures. For comparison, the linear thermal expansion data, obtained by dilatometry (d-LTEC) in our previous study, are also included [19]. The TECs in selected temperature ranges were calculated from both the d-LTEC and *in-situ* PXRD data. As can be seen in Table 1, the two sets of data match each other fairly well, with the TEC values obtained from d-LTEC being between that calculated from the lattice parameters a and c.

More interestingly, the TEC value for lattice parameter c is higher than that for lattice parameter a, especially in the high temperature range. This reveals an anisotropic thermal expansion behavior of the LSFCr-3 perovskite, which cannot be detected by dilatometry measurements. Extensive work on $La_{1-x}Sr_xFeO_{3-\delta}$ perovskite materials has shown that the chemical expansion induced by the reduction of the Fe cation at high temperatures is the primary cause of this anisotropic expansion characteristic [23]. The anomalous slope change (at ~ 475 °C) in Fig. 1(c)-4 also provides evidence of the chemical

expansion of the LSFCr-3 material. Given the above considerations, the thermal expansion behavior of the LSFCr-3 perovskite is due to "pure" thermal expansion and chemical expansion, which can be distinguished by the anisotropic expansion of the crystal lattice.

3.2. Stoichiometry of LSFCr-3 perovskite

In our previous study, the chemical (structural) stability, thermal expansion, electrical conductivity, and electrocatalytic properties of $La_{0.3}Sr_{0.7}Fe_{1-x}Cr_xO_{3-\delta}$ (x = 0, 0.1, 0.2 and 0.3, respectively) were investigated over a wide range of pO_2 values and temperatures. The trade-offs between these characteristics have led to the identification of the LSFCr-3 material as having the optimum composition within the $La_{0.3}Sr_{0.7}Fe_{1-x}Cr_xO_{3-\delta}$ family (when $x > 0.33$, impurity peaks corresponding to the $SrCrO_4$ phase appear) [19]. Considering that Cr can evaporate during the high temperature annealing, it was necessary to determine the stoichiometry of LSFCr-3 in the as-synthesized form (after annealing at 1200 °C for 2 h in air). For this purpose, the cation stoichiometry of the LSFCr-3 oxide was determined by ICP-MS analysis, giving a compositional formula of $La_{0.34(1)}Sr_{0.66(8)}Fe_{0.70(0)}Cr_{0.29(3)}$. This result is consistent with what was expected from the nominal composition ($La_{1/3}Sr_{2/3}Fe_{0.7}Cr_{0.3}$) and rules out the possibility of extensive Cr evaporation during the calcination process.

In order to then determine the anion stoichiometry (δ values) and obtain the exact chemical composition of the LSFCr-3 oxide at various temperatures, TG analysis was carried out in air, with the results shown in Fig. 2. An obvious weight loss commences at approximately 400 °C, which is generally in agreement with the temperature corresponding to the anomalous slope change in Fig. 1(b)-4. This result implies that the B-site cations in the LSFCr-3 perovskite start to be thermally reduced at 400 °C. The δ value at room temperature (δ_0), determined by iodometric titration, was 0.1 for the as-synthesized sample in air, while it gradually increases with temperature and reaches a value of 0.19 at 800 °C. Therefore, the stoichiometries of the LSFCr-3 perovskite was confirmed to

be $La_{0.34}Sr_{0.67}Fe_{0.70}Cr_{0.29}O_{2.9}$ and $La_{0.34}Sr_{0.67}Fe_{0.70}Cr_{0.29}O_{2.81}$ at room temperature (RT) and 800 °C, respectively.

3.3. Oxidation state of B-site cations (Fe and Cr) in LSFCr-3 perovskite

Mössbauer spectroscopy is unique in its sensitivity to subtle alterations in the chemical environment of a nucleus, such as oxidation state changes. This technique, which was carried out at room temperature, is also able to selectively indicate the oxidation state of cations in the bulk of solid materials using gamma-ray sources, especially for Fe cations [24]. Fig. 3 shows the room temperature Mössbauer spectrum of the LSFCr-3 powder and its Lorentzian profile fit. The resulting parameters after peak fitting, including the isomer shift (IS), peak attribute, peak area and molar fraction of Fe cation, are displayed in the inset. The spectrum profile is similar to what was reported for the $La_{1-x}Sr_xFeO_3$ (x= 0.7-0.9) compounds at 295 K, and corresponds to a paramagnetic phase, with the spectrum easily fitted by two singlets [25].

The oxidation state of Fe can be determined by the observed range of the IS values. The IS value for high-spin Fe^{2+}, Fe^{3+}, Fe^{4+} and Fe^{6+} ions lies in the range of 0.6 to 1.7 mm•s^{-1}, 0.1 to 0.6 mm•s^{-1}, -0.2 to 0.2 mm•s^{-1}, and -0.8 to -0.9 mm•s^{-1}, respectively [24]. In Fig. 3(a), the IS values of 0.064 and 0.39 mm•s^{-1}, associated with singlets, fall well within the characteristic range for Fe^{4+} and Fe^{3+}, respectively, ruling out the presence of Fe^{2+} in the bulk of the LSFCr-3 perovskite. According to the peak areas of the singlet curves, the concentration of Fe^{4+} and Fe^{3+} is calculated to be 50.5% and 49.5%, respectively, at room temperature. The chemical formula of the LSFCr-3 material is thus, more correctly, $La_{0.34}Sr_{0.67}(Fe^{3+}_{0.346}Fe^{4+}_{0.354}Cr^{3.4+}_{0.29})O_{2.9}$, at room temperature, with the average valence of the Cr cation then being determined to be +3.4, based on the charge neutrality of this compound.

Theoretically, the +3.4 average oxidation state of Cr in the LSFCr-3 oxide could arise from any combination of Cr^{3+}, Cr^{4+} and Cr^{6+}, but with a majority of Cr^{3+} being present. Here, two combinations, Cr^{3+}/Cr^{4+} and Cr^{3+}/Cr^{6+}, were assumed to be the majority species. According to the

stoichiometry (0.29) and total charge (+0.968 = +3.4×0.29) associated with the Cr cation, its specific oxidation states and concentration were shown to be $Cr^{3+}_{0.174}Cr^{4+}_{0.116}$ and $Cr^{3+}_{0.257}Cr^{6+}_{0.033}$ for each combination. Consequently, the chemical formula of the LSFCr-3 material (in the bulk) is further suggested to be either $La_{0.34}Sr_{0.67}(Fe^{3+}_{0.346}Fe^{4+}_{0.354}Cr^{3+}_{0.174}Cr^{4+}_{0.116})O_{2.9}$ or $La_{0.34}Sr_{0.67}(Fe^{3+}_{0.346}Fe^{4+}_{0.354}Cr^{3+}_{0.257}Cr^{6+}_{0.033})O_{2.9}$ at room temperature.

In order to then determine the oxidation state of the B-site cations under SOFC operating temperatures, *in-situ* high temperature XPS measurements were performed on the dense LSFCr-3 samples from room temperature to 700 °C. The low resolution survey scans spectra (Fig. S1, Supporting Information) show the presence of the elements in the LSFCr-3 material at each temperature from the $La3d_{5/2}$, Fe2p, Cr2p, Sr3d, O1s and C1s photoelectron energies, respectively. The C1s peak was assigned to adventitious carbon and was used to calibrate the experimentally obtained binding energies.

The result of the XPS survey spectrum analysis is in good agreement with the elementary composition of the oxide material. The height of the peaks associated with the LSFCr-3 phase at elevated temperatures is larger than that at room temperature. This was attributed to the progressive desorption of adventitious carbon at high temperatures, which is consistent with the reduction in the height of the C1s peak at 285 eV.

Fig. 4 shows the high resolution O1s, Fe2p and Cr2p spectra, collected from room temperature to 700 °C. The XPS spectra of $La3d_{5/2}$ and Sr3d are displayed in Fig. S2 (Supporting Information), indicating a constant oxidation state of both of these elements, as expected, and only a subtle change with increasing temperature is seen [26]. In contrast, the O1s peak changes notably when the temperature increases from RT to 300 °C, with peak (1) at 531.47 eV becoming very weak at elevated temperatures. As reported previously [27], the O 1s peak at 528.70 eV is attributed to normal lattice oxygen (O_L) in the perovskite structure, corresponding to peak (2) in Fig. 4(a). In addition, the

O1s peaks at 530.50, 531.45, and 532.35 eV are assigned to chemisorbed oxygen (O_C) in the forms of O^{2-}, O^- and O_2^-, respectively. These generally correspond to peak (1) in Fig. 4(a) and were derived from the trapping of mobile electrons of the LSFCr-3 ceramic by absorbed molecular oxygen and dissociated oxygen atoms.

Therefore, the decreasing intensity of peak (1) indicates a marked decrease in the O_C concentration on the LSFCr-3 surface with elevated temperatures. This result implies that the concentration of mobile electrons (charge carriers) in the LSFCr-3 material decreases significantly with increasing temperature. This is consistent with our previous work on the electrical conducting behavior of this material and also infers a relationship between the chemical state of oxygen on the surface and the electrical nature of the ceramic [19].

It was difficult to quantitatively interpret the Fe 2p peaks due to the small chemical shift of only 0.5 eV between Fe^{3+} and Fe^{4+} [28]. The satellite peaks for Fe $2p_{3/2}$ (≈ 718.40 eV) are clearly distinguishable in all of the spectra, while the binding energy is sensitive to the oxidation state of the Fe cation. As reported by other researchers [29, 30], a satellite peak at approximately 8.0 eV above the primary Fe $2p_{3/2}$ peak is characteristic of an Fe^{3+} species, while a satellite at approximately 6.0 eV above the Fe $2p_{3/2}$ peak is characteristic of Fe^{2+}. These data thus indicate that there is a small amount of Fe^{2+} on the surface of the LSFCr-3 material at all temperatures. Combining all of the results (oxidation state of the Fe cation) for the bulk of the perovskite, obtained by Mössbauer spectroscopy, with the XPS surface analysis data, it can be concluded that the Fe cations are present primarily as Fe^{3+} and Fe^{4+} from the surface through to the bulk of the LSFCr-3 material.

The Cr 2p peaks in Fig. 4(c) suggest that at least two distinct valence states of Cr are present on the surface of LSFCr-3, with the $Cr2p_{3/2}$ spectra clearly splitting into two peaks at all temperatures. Based on the binding energy of Cr cations in a range of Cr compounds in the literature [31, 32], the $Cr2p_{3/2}$ peak at 579.94 eV is attributed to Cr^{6+}, while the Cr $2p_{3/2}$ peak at 577.20 eV is assigned to Cr^{3+} (or Cr^{4+}).

As the temperature increases, a change in intensity of both the Cr^{6+} and Cr^{3+} (Cr^{4+}) peaks is seen in Fig. 4(c). However, these need to be fitted to allow for quantitative analysis. Fig. 5 shows the typical fitting pattern of the Cr2p peak for the LSFCr-3 sample collected at 500 ^{o}C using a step size of 0.1 eV (Fig. S3 shows the fitting patterns at room temperature, 300 ^{o}C, 600 ^{o}C and 700 ^{o}C). The sample was kept at each temperature for 4 h prior to the measurements. The Shirley Algorithm was used to estimate the background of the spectra and a Gaussian-Lorentzian line shape GL(30) was employed to fit the XPS peaks. The area ratio of the Cr $2p_{3/2}$ and Cr $2p_{1/2}$ peaks should be 2:1, based on the multiplicity of the state for p electrons [33].

At room temperature, Table 2 shows that the atomic ratio of the Cr^{6+} to Cr^{3+} ions (or Cr^{4+}) is approximately 1, implying that the concentration of Cr^{6+} on the surface of the LSFCr-3 perovskite is much higher than it is in the bulk, which was shown by Mössbauer spectroscopy to be < 0.1 ($Cr^{3+}_{0.174}Cr^{4+}_{0.116}$ or $Cr^{3+}_{0.257}Cr^{6+}_{0.033}$). This can be explained by (1) the formation of a thin layer of $SrCrO_4$ phase, which cannot be detected by XRD, on the surface of the LSFCr-3 material, or (2) the Cr species are stabilized in the +6 oxidation state at the LSFCr-3 perovskite surface. As the temperature increases to 500 ^{o}C, the amount of Cr^{6+} gradually increases with increasing pO_2 in the XPS chamber, as expected. The pO_2 values were calculated as a function of temperature, using the pressure within the XPS heating chamber.

As the temperature was increased from 500^{o}C to 700 ^{o}C, the pO_2 within the XPS heating chamber increased slightly (Table 2). The observed decrease in the Cr^{6+} content with increasing temperature can be attributed to oxygen loss, accompanied by the reduction of Cr^{6+} to Cr^{3+}(Cr^{4+}) on the surface of the LSFCr-3 perovskite. Furthermore, as can be seen in Table 2, the pO_2 inside the XPS chamber at 500-700 ^{o}C is on the order of 10^{-10} atm, which is very low compared to the ca. 0.21 atm environment experienced by an operating SOFC cathode. However, for the XPS measurements, high vacuum conditions are normally required in order to be able to collect the electrons. Therefore, the results

obtained by these *in-situ* (high temperature) XPS measurements are suggested to represent the oxidation state of each element in the LSFCr-3 perovskite under severe cathodic polarization (high current operation), when the oxygen would be depleted at the active sites and its reduction rate would be diffusion controlled.

3.4. Electrical conductivity of LSFCr-3 perovskite

In our previous study, the electrical conductivity of the LSFCr-3 oxide was investigated as a function of temperature in air [19]. Due to the relatively low mobility of oxygen anions (two or three orders of magnitude lower than that of the electron and holes), the measured electrical conductivity can be regarded as representative of the electronic conductivity [34]. However, in order to understand the electro-catalytic activity of the LSFCr-3 cathodes, it is also very useful to know their ionic conductivity.

For this purpose, a Brouwer diagram of the LSFCr-3 perovskite was examined (Fig. 6), in which logarithmic plots of the equilibrium total conductivity versus the logarithm of pO_2 at different temperatures are presented. The pO_2 test range was selected to be within the structural stability limit of the LSFCr-3 perovskites, which was determined by *in-situ* XRD studies in our previous work [19]. Here, the complex character of the plots in Fig. 6 is suggested to reflect changes in the concentration of the various charge carriers as a function of pO_2. At the high-pressure limit (10^{-6} - 1 atm), the data at various temperatures can be fitted to a straight line with a slope of ca. 1/6 (Table 3), indicating a predominantly p-type conducting behavior of LSFCr-3 in the high pO_2 range [34]. In the medium-pressure range (10^{-6} - 10^{-13} atm), it was difficult to obtain reliable data, due to the slow equilibration kinetics between the specimen and environment.

At still lower pressures ($pO_2 < 10^{-13}$), the electrical conductivity of the specimens (Fig. 6) exhibits the same variation with pO_2 over a range of temperatures, decreasing with pO_2 down to a minimum value and then increasing again. These types of minima in conductivity are typical of oxides when

the pO_2 variations at constant temperature result in nearly equal concentrations of electron- and hole-like carriers in the material [34]. The presence of ionic current, which is almost pO_2 independent at the low-pressure limit, is responsible for the smooth shape of the curve near the conductivity minima (Fig. 6). Based on these arguments, the experimental results near the conductivity minima were fitted approximately to the following equation [35]:

$$\sigma = \sigma_i + \sigma_n^o \cdot pO_2^{-1/4} + \sigma_p^o \cdot pO_2^{+1/4} \quad (2)$$

where σ_i represents the oxygen ion contribution and, σ_n^o and σ_p^o represent the electron and hole contributions to the total conductivity, respectively. The fitting parameters that enabled a satisfactory approximation of the experimental data are given in Table 3. The ionic conductivity of the LSFCr-3 specimens is in the range of 10^{-2} S·cm^{-1} at 700-800 °C, which is comparable to that of the YSZ electrolyte [36].

As is generally recognized, when pO_2 varies from the high-pressure extreme to the low-pressure limit, there should be a significant increase in the number of oxygen vacancies in the perovskites, resulting in a change in ionic conductivity [34]. Consequently, σ_i (Table 3) obtained at the low pO_2 limit, could be different from that for the LSFCr-3 perovskite under typical cathode operating conditions (high pO_2 limit, 0.1-0.21 atm). An alternative way to precisely determine the ionic conductivity of the LSFCr-3 material is to measure the oxygen anion diffusion coefficient in air.

The DC conductivity relaxation technique was therefore employed for this purpose. Fig. 7(a) demonstrates the total electrical conductivity response between 700 and 800 °C upon abruptly changing the pO_2 from 0.1 to 0.21 atm. During the oxidation step (when pO_2 increases from 0.1 to 0.21 atm), oxygen anions are incorporated into the crystal lattice of the LSFCr-3 material, resulting in a transient increase in the oxygen stoichiometry (δ). This can be described by Fick's second law,

where the value of the chemical diffusion coefficient, $\tilde{\tilde{D}}$, is evaluated by non-linear-least-square fitting of the conductivity relaxation data to the following equation [37]:

$$\frac{\sigma(t)-\sigma(0)}{\sigma(\infty)-\sigma(0)} = 1 - \sum_{n=1}^{\infty} \frac{2L^2 \exp(-\beta_n^2 \tilde{\tilde{D}} t / l^2)}{\beta_n^2 (\beta_n^2 + L^2 + L)} \quad (3)$$

where β_n is obtained from equation (4),

$$\beta_n \tan \beta_n = \frac{lk}{\tilde{\tilde{D}}} = L \quad (4)$$

and where $\sigma(0)$, $\sigma(t)$ and $\sigma(\infty)$ represent the equilibrium total conductivity at t = 0 (initial), at time t (during the relaxation), and at $t \rightarrow \infty$ (after reaching a new equilibrium state), respectively, k is the surface exchange coefficient, and l is the half thickness of the sample [37].

The normalized relaxation profiles of the total conductivity and the fitting curves are shown in Fig. 7(b). From these results, the values of $\tilde{\tilde{D}}$ and k at 700-800 °C were obtained and are displayed in Table 4. As can be seen, both $\tilde{\tilde{D}}$ and k are found to increase with increasing temperature, agreeing well with what has been reported previously for many other mixed conducting perovskites [16, 38].

When the total electrical conductivity of a mixed conductor is predominantly determined by the electronic contribution, bulk transport is controlled by ionic diffusion [34]. Consequently, the self-diffusion coefficient can be calculated from $\tilde{\tilde{D}}$ for LSFCr-3 using this relationship [39]:

$$D_o^* = \frac{\tilde{\tilde{D}}}{\gamma} \quad (5)$$ where

γ represents the thermodynamic factor:

$$\frac{1}{\gamma} = \frac{2\partial \ln C_O}{\partial \ln pO_2} = \frac{2 \lg e}{3-\delta} \times \frac{d\delta}{d \lg pO_2} \quad (6)$$

with the oxygen concentration being $C_O = \frac{(3-\delta)}{V_m}$, V_m being the molar volume of the unit cell (V_m=N×V), N Avogadro's number, and V being the unit cell volume over a range of temperatures. From an experimental point of view, the $\frac{d\delta}{d \lg pO_2}$ values can be obtained as a function of temperature from thermogravimetric analysis (Fig. 8), then giving the γ and D_o^* values.

The ionic conductivity of any material can be calculated using the Nernst-Einstein equation 7 [39]:

$$\sigma_O = \frac{z_o^2 F^2 D_O^* C_O}{RT} \qquad 7$$

where $z_o F$ represents the electrical charge of 1 mole of oxygen ions and F is the Faraday constant. The resulting σ_O values for the LSFCr-3 material are 0.032, 0.011 and 0.004 S·cm^{-1} at 800 °C, 750 °C and 700 °C, respectively, which is a little smaller than the values deduced from the Brouwer diagram at the low pO_2 limit (Table 3).

In addition, it is seen that the σ_O and k values for the LSFCr-3 perovskite are comparable to those for high performing $La_{1-x}Sr_xCo_yFe_{1-y}O_{3-\delta}$ cathodes with a high Co content [38, 40, 41]. This result rules out the formation of even a thin layer of $SrCrO_4$ (in which Cr would be in the +6 state) on the surface of the LSFCr-3 perovskite, as $SrCrO_4$ is known to have poor electrical conductivity and electrocatalytic activity toward the oxygen redox reaction [21]. As has been generally recognized, the oxidation state of the B-site transition metal cations governs the electrocatalytic activity of perovskite-based cathodes. In terms of our analysis (Section 3.3) of the oxidation state of the B-site Fe and Cr cations (from the surface through to the bulk of the LSFCr-3 material), the rapid oxygen bulk diffusion and high surface exchange rate (Table 4) of the LSFCr-3 material are both assumed to be related primarily to the contribution of the Cr cations. These were shown above to be predominantly in the 3+ and 4+ oxidation state in the bulk of LSFCr-3, as Cr has a strong preference

for maintaining a 6-fold coordination with oxygen anions. This, in turn, causes disorder in the oxygen vacancy sub-lattice, which is stabilized by Fe ions (iron-oxygen tetrahedral), resulting in very good oxygen ionic conductivity (bulk diffusion) within the LSFCr-3 material.

On the surface of LSFCr-3, the Cr cation valence was shown to be unexpectedly high, with the atomic ratio of Cr^{6+} to Cr^{3+} (Cr^{4+}) being approximately 1, even at 700 °C (Table 2). According to the oxidation state and coordination requirements of transition metal ions, Cr^{6+} can only be tetrahedrally coordinated by the oxygen anions [42], producing a large concentration of oxygen vacancies on the surface of LSFCr-3. In general, the more oxygen vacancies present, the more rapidly oxygen can be absorbed and dissociatively reduce on the surface, and then move into an oxide lattice for a given chemical potential driving force [43]. Therefore, these segregated oxygen vacancies, caused by the formation of Cr^{6+} on the LSFCr-3 surface, are suggested to be responsible for the excellent k values (Table 4) observed. This is therefore the first time that a highly beneficial effect of Cr on the electrical characteristics of a perovskite-based mixed conductor (LSFCr-3) is being reported. Much more typically, Cr exhibits a harmful effect on these types of materials by lowering their oxygen ionic conductivity and chemically reacting with the A-site or B-site cations (e.g., Cr poisoning of some SOFC cathodes) [44, 45]. In our future work, angle resolved XPS data on LSFCr-3 thin films and density functional theory (DFT) calculations will be performed to obtain more insights into the mechanism of formation of the high oxidation state of Cr (Cr^{6+}) on the surface of our LSFCr-3 material.

Given the above considerations, it should not be not surprising that the electrochemical performance of the LSFCr-3 cathode is superior (As reported previously [19] and shown below) to what has been reported previously for LSCF with a low-Co content [20].

3.5. Oxygen redox reaction at LSFCr-3 perovskites

The electrocatalytic activity of the LSFCr-3 material toward the oxygen redox reaction (oxygen reduction reaction and oxygen evolution reaction, both occurring at the open circuit potential (OCP))

was determined by measuring the impedance of symmetrical half cells in air. Fig. 9 shows the impedance spectra of symmetrical LSFCr-3|LDC|LSGM|LDC|LSFCr-3 half-cells (where LSGM represents the $La_{0.8}Sr_{0.2}Ga_{0.8}Mg_{0.2}O_{3-\delta}$ electrolyte and LDC is $La_{0.4}Ce_{0.6}O_{2-\delta}$) at 750 °C in air at the OCP. The intercept of the impedance arcs with the real axis at high frequency corresponds to the ohmic resistance (R_{ohm}) associated with the electrolyte, contact and leads, while the full diameter of the arcs corresponds to the polarization resistance (R_p), which is inversely to the electrochemical reaction rates in the cell [46].

To obtain more insight into the oxygen redox reaction at the LSCFr-3/electrolyte interface, a study of the influence of the pO_2 and the applied DC bias on the electrode impedance was conducted at 750 °C (Fig.10). It is well known that the oxygen redox reaction at mixed conducting electrodes involves many processes, such as gas diffusion, surface adsorption, gas dissociation, electron and ion transport, charge transfer at the interface, and so on. Each of these processes has a different dependence on pO_2 [47]. The most commonly used approach to identify the rate-determining step (rds) in the oxygen redox reaction is to examine the slope of R_p as a function of oxygen partial pressure, following the relation [48]:

$$\frac{1}{R_p} \propto pO_2^n \qquad 8$$

The n value is expected be 1, 1/2 or 1/4 if the molecular oxygen, atomic oxygen or electron (charge transfer) is involved in the rds, respectively [48].

As seen in Fig. 10(a), R_p gradually increases with decreasing pO_2, giving a ca. $pO_2^{1/4}$ dependency (n = 0.28). In addition, it can be clearly seen in Fig. 10(b) that R_p of the LSFCr-3-based half cells, obtained in air, decreases as the amplitude of the applied DC bias increases, indicating that the rds of the electrode reaction occurring in the cell is an electrochemical reaction, not a pure chemical, reaction [49, 50]. Consequently, the results obtained under varying pO_2 and DC biases suggest

that the rds of the oxygen redox reaction is the charge transfer process for the LSFCr-3 electrode at 750 °C in air.

To further analyze the OCP impedance data for the oxygen reduction/evolution reaction at 750 °C, the Nyquist plots of the LSFCr-3-based half-cell in air (Fig. 9) were fitted to an $LR_{ohm}(R_1Q_1)(R_2Q_2)$ equivalent circuit model, where R_1 represents the resistance of the charge transfer process (rds) at higher frequencies and R_2, obtained from the low frequency arc, represents the O_2 dissociation and mass transfer processes. L is an inductance, seen only at very high frequencies and caused by the potentiostat and cables, while the Qs represents constant phase elements. The impedance, Z_Q, and the equivalent capacitance, C, of a Q parameter can be calculated according to the following equations [51]:

$$Z_Q = \frac{1}{Q(i\omega)^n} \quad (9)$$

$$C = \frac{(R^1Q)^{1/n}}{R} \quad (10)$$

where ω is the angular frequency and n is an exponent, where Q, represents an ideal capacitor and an ideal resistor when n = 1 and n = 0, respectively. When 0 < n < 1, this reflects the presence of inhomogeneities within the electrode system.

The electrode process corresponding to the high frequency (R_1Q_1) time constant has an equivalent capacitance of ca. 4.9×10^{-3} F•cm^{-2}, which is similar to that obtained in our previous work with $La_{0.3}Ca_{0.7}Cr_{0.3}Fe_{0.7}O_{3-\delta}$ as an air electrode and is also in the typical range found for charge transfer processes at mixed conducting cathode materials [51-53]. Further, the low frequency arc exhibits a capacitance value as large as 0.11 F•cm^{-2}, similar to what was obtained at a pO_2 of 0.04 atm (Fig. 10(a)). A capacitance of this magnitude (> 0.1 F •cm^{-2}) is not ascribable to an interfacial capacitance or adsorption on surfaces [54].

To date, two processes have been reported to give such a large capacitance at low frequencies. One originates from the change of the oxygen non-stoichiometry in mixed conductors when the electrode potential is varied, i.e., when the bulk oxidation state of the transition metals changes, called a "chemical capacitance" [43]. A second process that could give rise to such a large capacitance at low frequencies is oxygen gas diffusion [48], which could dominant the oxygen redox reaction when the cathode is starved of oxygen. As previously reported, the oxygen exchange reaction (chemical capacitance) is thermally activated, while gas diffusion should be almost temperature-independent. In recent parallel work, we have found that the low frequency resistance of LSFCr-3 has a pronounced temperature dependence, indicating that this feature is due to the change in redox state (chemical capacitance), likely of the Fe component, within this MIEC oxide [55].

3.6. Performance of LSFCr-3 cathodes in a Ni-$Ce_{0.8}Sm_{0.2}O_{2-\delta}$ (SDC) supported cell

In order to evaluate the cathode performance under more practical conditions, a LSFCr-3 cathode layer, with a thickness of approximately 20 μm, was deposited on a YSZ/SDC bi-layer electrolyte membrane supported by a Ni-SDC cermet. The fabrication process and microstructural characteristics of the resulting coin cells have been reported in our previous work [20].

Fig. 11 shows the I-V and I-P characteristics of this anode-supported cell at 750 ˚C with 3%H_2O-H_2/air environment at the anode/cathode. It can be seen that the cell exhibits a maximum power density of 0.81 W•cm^2, which is higher than well-known LSCF cathode-based cells (0.73 W•cm^2 in our previous work [20]) when using the same anode-supported configuration. Furthermore, our previous work demonstrated good long-term stability of the LSFCr-3 cathode under typical operating conditions [19]. Therefore, the LSFCr-3 material is clearly a very promising and robust new cathode material for SOFC applications.

4. Conclusions

A novel Co-free cathode, $La_{0.3}Sr_{0.7}Fe_{0.7}Cr_{0.3}O_{3-\delta}$ (LSFCr-3), exhibiting the desired combination of high electrical conductivity, physical and chemical stability, and electrocatalytic activity, was systematically investigated for solid oxide fuel cell (SOFC) applications. The LSFCr-3 perovskite is shown to have a hexagonal crystal structure (R-3c), which is thermodynamically stable upon heating to 900°C in air. The exact composition of the bulk of the LSFCr-3 material is suggested to be either $La_{0.34}Sr_{0.67}(Fe^{3+}_{0.346}Fe^{4+}_{0.354}Cr^{3+}_{0.174}Cr^{4+}_{0.116})O_{2.9}$ or $La_{0.34}Sr_{0.67}(Fe^{3+}_{0.346}Fe^{4+}_{0.354}Cr^{3+}_{0.257}Cr^{6+}_{0.033})O_{2.9}$ at room temperature.

Under typical SOFC cathode conditions, the rapid oxygen bulk diffusion (10^{-2} S·cm^{-1}) and high surface exchange rate (10^{-5} cm·s^{-1}) of the LSFC-3 material are both assumed to be related primarily to the presence of the Cr cations. Cr has a strong preference to maintain a 6-fold coordination with oxygen anions, which, in turn, causes disorder in the oxygen vacancy sub-lattice, resulting in very good oxygen ionic conductivity (bulk diffusion) within the LSFCr-3 material. The segregated oxygen vacancies, arising from the Cr^{6+} oxidation state at the surface, are suggested to be responsible for the very high k values obtained for the LSFCr-3 perovskite. This is therefore the first time that a beneficial effect of Cr on the electrical characteristics of a perovskite-based mixed conductor (LSFCr-3) is being reported.

In a symmetrical half-cell configuration based on the LSFCr-3 electrode material, a promising open circuit polarization resistance of only 0.25 Ω•cm^2 was achieved at 750 °C in air. The rate determining step of the oxygen redox reaction at LSFCr-3 at under these conditions is likely the electron charge transfer process. When LSFCr-3 was used as the cathode in a Ni-SDC anode-supported full cell, a maximum power density of 0.81 W•cm^2 was obtained, which is higher than what has been reported when the widely used LSCF cathode was used in a similar anode-supported

configuration. The LSFCr-3 material is clearly a very promising and robust new cathode material for use in SOFCs. .

Acknowledgements

Grateful acknowledgements are extended to Carbon Management Canada (a Canadian National Centre of Excellence), the Institute for Sustainable Energy, Environment and Economy (ISEEE) at the University of Calgary, as well as the SOFC Canada NSERC Strategic Research Network for covering the costs associated with this work.

Supporting Information

Table S1 : Electrical conductivity, average thermal expansion coefficients, and area specific resistance of a range of iron-based perovskite electrodes with the B-site iron lightly substituted by a high valence transition metal.

Figure S1 and S2 : Low resolution (full range survey scan) and high resolution (La 3d5/2 and Sr 3d) XPS spectra of the LSFCr-3 specimen collected from room temperature to 700 ^{o}C,

Figure S3: Fitting patterns of Cr 2p3/2 spectrum obtained for LSFCr-3, collected from room temperature to 700 ^{o}C.

References

(1) F.S. Baumann, J. Fleig, M. Konuma, U. Starke, H.U. Habermeier, J. Maier, *J. Electrochem. Soc.*, 2005, **152(10)**, A2074-A2079.

(2) M. Zhi, S. Lee, N. Miller, N.H. Menzlerd, N. Wu, *Energy Environ. Sci.*, 2012, **5**, 7066-7071.

(3) Z. Shao, S.M. Haile, *Nature*, 2004, **431**, 170-173.

(4) J. Peña-Martínez, D. Marrero-López, J.C. Ruiz-Morales, B.E. Buergler, P. Núñez, L.J. Gauckler, *Solid State Ionic*, 2006, **177**, 2143-2147.

(5) J.H. Kim, A. Manthiram, *J. Electrochem. Soc.*, 2008, **155(4)**, B385-B390.

(6) A. Aguadero, J.A. Alonso, D. Pérez-Coll, C.D.L. Calle, M.T. Fernández-Díaz, J.B. Goodenough, *Chem. Mater.*, 2010, **22**, 789-798.

(7) G. Xiao, Q. Liu, F. Zhao, L. Zhang, C. Xia, F. Chen, *J. Electrochem. Soc.*, 2011, **158(5)**, B455-B460.

(8) M. Bevilacqua, T. Montini, C. Tavagnacco, E. Fonda, P. Fornasiero, M. Graziani, *Chem. Mater.*, 2007, **19**, 5926–5936.

(9) H. Wang, C. Tablet, A. Feldhoff, J. Caro, *Adv. Mater.*, 2005, **17**, 1785–1788.

(10) C. Zhang, H. Zhao, *J. Mater. Chem.*, 2012, **22**, 18387–18394.

(11) J.A. Schuler, Z. Wuillemin, A. Hessler-Wyser, C. Comninellis, N.Y. Steiner, J.V. Herle, *J. Power Sources*, 2012, **211**, 177-183.

(12) T. Suzuki, Y. Funahashi, T. Yamaguchi, Y. Fujishiro, M. Awano, *J. Power Sources*, 2008, **175**, 68-74.

(13) D.M. Bastidas, S. Tao, J. T. S. Irvine, *J. Mater. Chem.*, 2006, **16**, 1603-1605.

(14) A. Sin, E. Kopnin, Y. Dubitsky, A. Zaopo, A.S. Aricò, L.R. Gullo, D.L. Rosa, V. Antonucci, *J. Power Sources*, 2005, **145**, 68-73.

(15) T. Ishihara, *Perovskite Oxide for Solid Oxide Fuel Cells*, Springer, New York, 2009.

(16) F. Dong, Y. Chen, R. Ran, D. Chen, M.O., Tadé, S. Liu, Z. Shao, *J. Mater. Chem. A.*, 2013, **1**, 9781-9791.

(17)S. Huang, G. Wang, X. Sun, C. Lei, T. Li, C. Wang, *J. Alloys Compd.*, 2012, **543**, 26-30.

(18) A.J. Fernández-Ropero, J.M. Porras-Vázquez, A. Cabeza, P.R. Slater, D. Marrero-López, E.R. Losilla, *J. Power Sources*, 2014, **249**, 405-413.

(19) M. Chen, S. Paulson, V. Thangadurai, V. Birss, *J. Power Sources*, 2013, **236**, 68-79.

(20) M. Chen, B.H. Moon, S.H. Kim, B.H. Kim, Q. Xu, B.G. Ahn, *Fuel Cells*, 2012, **12(1)**, 86-96.

(21) V.L. Kozhevnikov, I.A. Leonidov, J.A. Bahteeva, M.V. Patrakeev, E.B. Miterg, K.R. Poeppelmeier, *Chem. Mater.*, 2004, **16**, 5014-5020.

(22) J.M. Haag, B.D. Madsen, S.A. Barnett, K.R. Poeppelmeier, *Electrochem. Solid-State Lett.*, 2008, **11(4)**, B51-B53.

(23) X. Chen, T. Grande, *Chem. Mater.*, 2013, **25**, 3296-3306

(24) D.P.E. Dickson, F.J. Berry, *Mössbauer spectroscopy,* Cambridge University Press, London, 1986.

(25) U. Shimony, J.M. Knudsen, *Phys. Rev*., 1966, **144(1)**, 361-366.

(26) G. Vovk,; X. Chen, C.A. Mims, *J. Phys. Chem. B*, 2005, **109**, 2445-2454.

(27) Q. Xu, D. Huang, W. Chen, H. Wang, B. Wang, R. Yuan, *Appl. Surf. Sci*., 2004, **228**, 110-114.

(28) A. Fujimori, T. Mizokawa, T. Saitoh, H. Namatame, S.Suga, N. Kimizuka, Y. Takeda, M. Takano, *Phys. Rev*. B, 1992, **45(4)**, 1561-1570.

(29) P. Mills, J.L. Sullivan, *J. Phys. D: Appl. Phys.*, 1983, **16**, 723-732.

(30) T. Yamashita, P. Hayes, *Appl. Surf. Sci*., 2008, **254**, 2441-2449.

(31) K. Rida, A. Benabbas, F. Bouremmad, M.A. Peña, A. Martínez-Arias, *Catal. Commun.*, 2006, **7**, 963-968.

(32) X. Liu, W. Su, Z. Lu, J. Liu, L. Pei, W. Liu, L. He, *J. Alloys Compd.*, 2000, **305**, 21-23.

(33) C. S. Fadley, D. A. Shirley, *J. Research of the National Bureau of Standards – A. Physics and Chemistry*, 1970, **74A**, 543-558.

(34) J. Sunarso, S. Baumann, J.M. Serra, W.A. Meulenberg, S. Liu, Y.S. Lin, J.C. Diniz da Costa, *J. Membrane. Sci.*, 2008, **320**, 13-41.

(35) V.L. Kozhevnikov, I.A. Leonidov, M.V. Patrakeev, E.B. Mitberg,; K.R. Poeppelmeier, *J. Solid State Chem.*, 2000, **158**, 320-326.

(36) S.C. Singhal, K. Kendall, High Temperature Solid Oxide Fuel Cells: Fundamentals, Design and Applications, Elsevier, UK, 2004.

(37) M.W. Den Otter, L.M. Van der Haar, H.J.M Bouwmeester, *Solid State Ionics*, 2000, **134**, 259-264.

(38) H.J.M. Bouwmeester, M.W. Den Otter, B.A. Boukamp, *J. Solid State Electrochem.*, 2004, **8**, 599-605.

(39) F. Mauvy, J.M. Bassat, E. Boehm, P. Dordor, J.C. Grenier, J.P. Loup, *J. Eur. Ceram. Soc.*, 2004, **24**, 1265-1269.

(40) R. Ganeshananthan, A.V. Virkar, *J. Electrochem. Soc.*, 2005, **152(8)**, A1620-A1628.

(41) J. Richter, P. Holtappels, T. Graule, T. Nakamura, L.J. Gauckler, *Monatsh. Chem.*, 2009, **140**, 985-999.

(42) H. S. Nalwa, *Handbook of Surfaces and Interfaces of Materials*, Academic Press, London, 2001.

(43) S.B. Adler, *Chem. Rev.*, 2004, **104**, 4791.

(44) M. Kornely, N.H. Menzler, A. Weber, E. Ivers-Tiffée, *Fuel cells*, 2013, **13(4)**, 506-510.

(45) K. Fujita, K. Ogasawara, Y. Matsuzaki, T. Sakurai, *J. Power Sources*, 2004, **131**, 261-269.

(46) J.R. Wilson, S.A. Barnett, *Electrochem. Solid State Lett.*, 2008, **11**, B181-B185.

(47) M.J. Escudero, A. Aguadero, J.A. Alonso, L. Daza, *J. Electroanal. Chem.*, 2007, **611**, 107-116.

(48) Y. Takeda, R. Kanno, M. Noda, Y. Tomida, O. Yamamoto, *J. Electrochem. Soc.*, 1987, **134(11)**, 2656-2661.

(49) M. Liu, Z. Wu, *Solid State Ionics*, 1998, **107**, 105-110.

(50) E. J. L., Schouler, M. Kleitz, *J. Electrochem. Soc.*, 1987,**134**, 1045-1050.

(51) B. Molero-Sánchez, J. Prado-Gonjal, D. Ávila-Brande, M. Chen, E. Morán, V. Birss, Int. J. Hydrogen Energy, 2015, **40**, 1902-1910.

(52) D. Chen, R. Ran, K. Zhang, J. Wang, Z. Shao, *J. Power Sources*, 2009, **188(1)**, 96-105.

(53) F. Mauvy, C. Lalanne, J.M Bassat, J.C. Grenier, H. Zhao, L. Huo, P. Stevens, *J. Electrochem. Soc.*, 2006, **153(8)**, A1547-A1553.

(54) Q. X. Fu, F. Tietz, D. Stöver, *J. Electrochem. Soc.*, 2006, **153(4)**, D74-D83.

(55) B. Molero-Sánchez, P. Addo, A. Buyukaksoy, S. Paulson, V. Birss, Faraday Discuss. Chem. Soc. 2015, *DOI: 10.1039/C5FD00029G*.

Figure captions

Fig. 1. (a) Powder X-ray diffraction (PXRD) Rietveld refinement of as-prepared LSFCr-3 at room temperature. Inset shows the idealized crystal structure of LSFCr-3, (b) shows the i*n-situ* XRD patterns for LSFCr-3 in air at 300-900 °C in the 2θ ranges of 31-34 ° and 45-48 ° , while (c) shows the resulting hexagonal lattice parameters (a and c) and the unit cell volume as a function of temperature. For comparison, linear thermal expansion data, measured by dilatometry in our previous study 19, are displayed in Fig. 1(c)-4.

Fig. 2. Thermogravimetric analysis (TGA) weight loss and oxygen non-stoichiometry (δ) of the LSFCr-3 powders as a function of temperature in air. A relatively low heating rate of 1 ^{o}C/min was used for the TG run.

Fig. 3. Mössbauer spectroscopy of the LSFCr-3 powders and the Lorentzian profile fit at room temperature. The resulting parameters after peak fitting, including isomer shift (IS), peak attribute, peak area and molar fraction of Fe cation, are shown in the inset.

Fig. 4. High resolution *in-situ* XPS (a) O1s La $3d_{5/2}$, (b) Fe 2p and (c) Cr 2p peaks collected from room temperature to 700 ^{o}C, respectively.

Fig. 5. Typical fitting patterns of Cr $2p_{3/2}$ spectrum for the LSFCr-3 specimen, with the data collected at 500 ^{o}C.

Fig. 6. Logarithmic plots of total electrical conductivity versus oxygen partial pressure (pO_2) for the LSFCr-3 specimen at 700-800 °C.

Fig. 7. (a) Total electrical conductivity and (b) Normalised conductivity relaxation plots for the LSFCr-3 specimens at 700-800 °C upon abruptly changing the pO_2 from 0.1 to 0.21 atm.

Fig. 8. Oxygen nonstoichiometry (δ) of the LSFCr-3 material as a function of pO_2 at 700-800 °C. Inset shows the specific values of $\frac{d\delta}{d \lg pO_2}$.

Fig. 9. Nyquist and Bode (inset) impedance plots of the LSFCr-3-based symmetrical half cells measured in air at 750 °C at the open circuit potential (OCP).

Fig. 10. The effect of (a) pO_2 and (b) applied DC bias on the impedance spectra of the LSFCr-3-based symmetrical half cells at 750 °C. Inset in (a) shows the dependence of the polarization resistance (R_p) on the pO_2, while the inset in (b) shows the corresponding impedance spectra in the Bode mode.

Fig. 11. Potential and power density plots of the LSFC-3 material as a cathode in a Ni-SDC anode-supported cell, measured at 750 °C with wet (3%H_2O)-H_2 as the fuel and air as the oxidant.

Tables

Table 1. Average thermal expansion coefficients over various temperature ranges for LSFCr-3 material, determined by *in-situ* PXRD and dilatometry measurements.

Thermal expansion parameters	Average TEC ($\times 10^{-6} \bullet K^{-1}$)	
	Full temperature range	High temperature range
Lattice parameter (a)	15.7 (25-900 °C)	18.1(500-900 °C)
Lattice parameter (c)	17.1 (25-900 °C)	22.6 (500-900 °C)
Linear thermal expansion (dilatometer)	16.3 (50-900 °C)	21.1 (500-900 °C)

Table 2. Parameters determined from the fitting patterns of Cr 2p3/2 XPS spectrum at various temperatures.

Temperature	pO_2 (atm)	Attribute	BE (ev)	FWHM (ev)	Peak Area	Atomic ratio
R.T.	8.3×10^{-13}	Cr^{6+}	579.53	2.01	1009.97	50.20%
		Cr^{3+}(or Cr^{4+})	577.00	2.35	1001.79	49.80%
300 °C	2.1×10^{-12}	Cr^{6+}	579.61	2.05	1922.49	55.20%
		Cr^{3+}(or Cr^{4+})	576.99	2.24	1560.40	44.80%
500 °C	1.0×10^{-10}	Cr^{6+}	579.83	1.90	2465.41	63.20%
		Cr^{3+}(or Cr^{4+})	577.12	2.26	1435.41	36.80%
600 °C	1.2×10^{-10}	Cr^{6+}	579.95	1.83	2035.58	52.53%
		Cr^{3+}(or Cr^{4+})	577.15	2.68	1839.88	47.47%
700 °C	1.7×10^{-10}	Cr^{6+}	579.99	2.15	1950.58	50.86%
		Cr^{3+}(or Cr^{4+})	576.94	2.71	1884.42	49.14%

*BE represents binding energy and FWHM represents full width at half maximum.

Table 3. Slope of linear fitting in the high pO_2 limit (10^{-6} - 1 atm) and conductivity parameters obtained by fitting equation (2) to experimental data in the low pO_2 limit (<10^{-13} atm).

Parameter	Temperature (°C)		
	800	750	700
Slope of linear fitting	1.5×10^{-1}	1.4×10^{-1}	1.4×10^{-1}
$\sigma_i\ (S\cdot cm^{-1})$	4.9×10^{-2}	2.4×10^{-2}	1.1×10^{-2}
$\sigma_n^o(S\cdot cm^{-1}\cdot atm^{-1/4})$	1.7×10^{-6}	4.8×10^{-7}	1.8×10^{-7}
$\sigma_p^o(S\cdot cm^{-1}\cdot atm^{1/4})$	2.7×10^{3}	4.8×10^{3}	9.6×10^{3}

Table 4. Oxygen diffusion coefficient ($\tilde{\tilde{D}}$) and surface exchange coefficient (k) of the LSFCr-3 specimens estimated by fitting equation 3 to the normalised conductivity relaxation plots at 700-800 °C.

$Temperature(^\circ C)$	$\tilde{\tilde{D}}(cm^2\cdot s^{-1})$	$k(cm\cdot s^{-1})$
800	5.0×10^{-5}	6.7×10^{-5}
750	2.0×10^{-5}	4.8×10^{-5}
700	8.0×10^{-6}	4.2×10^{-5}

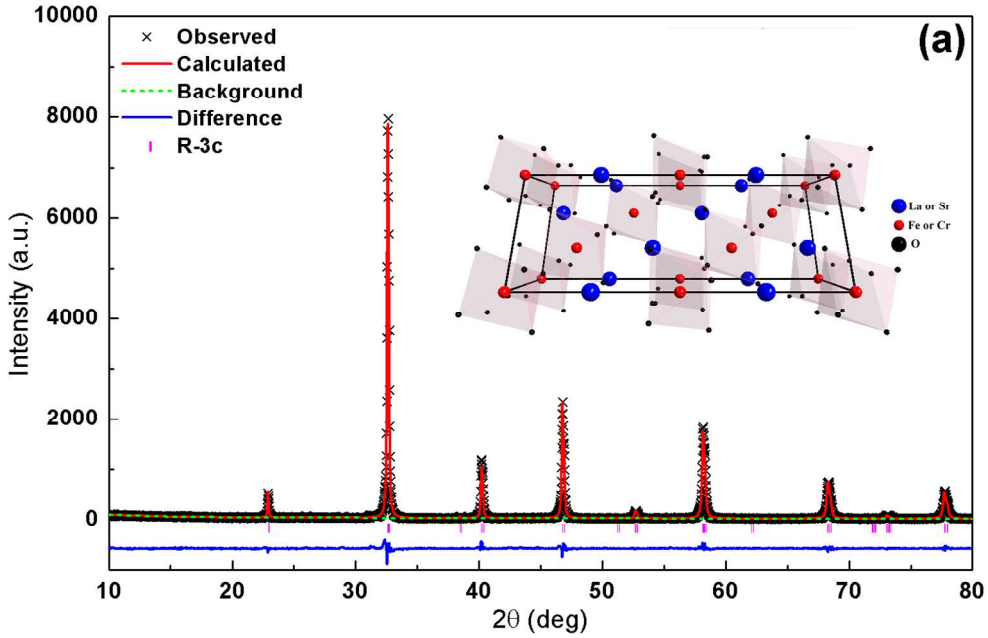

269x172mm (150 x 150 DPI)

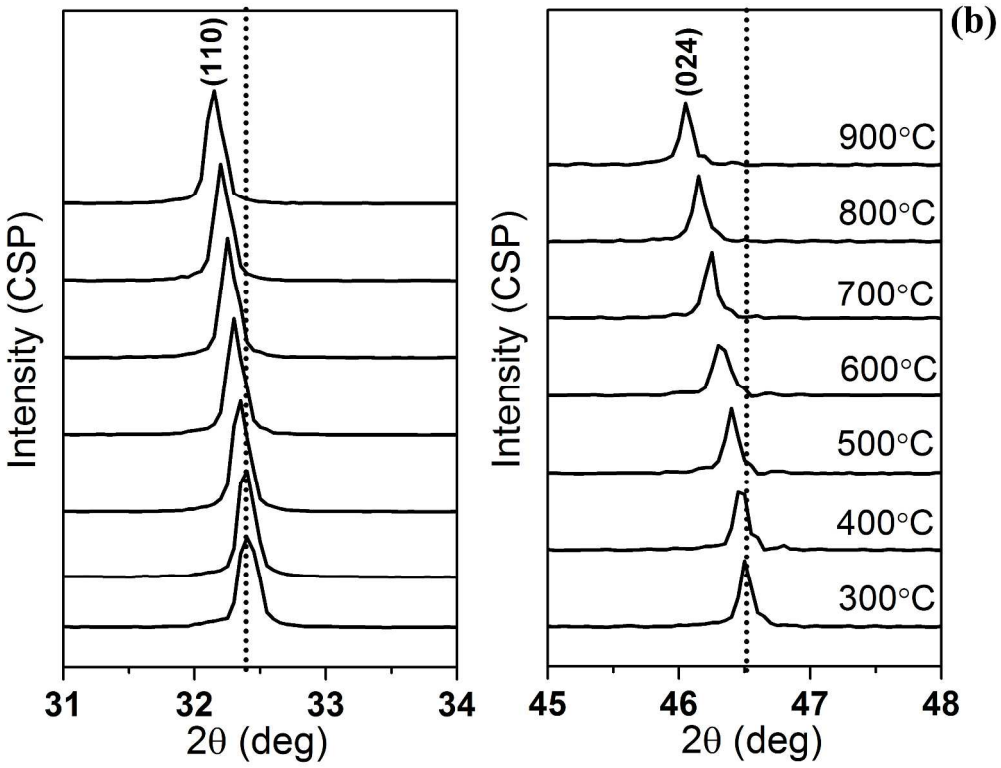

330x252mm (300 x 300 DPI)

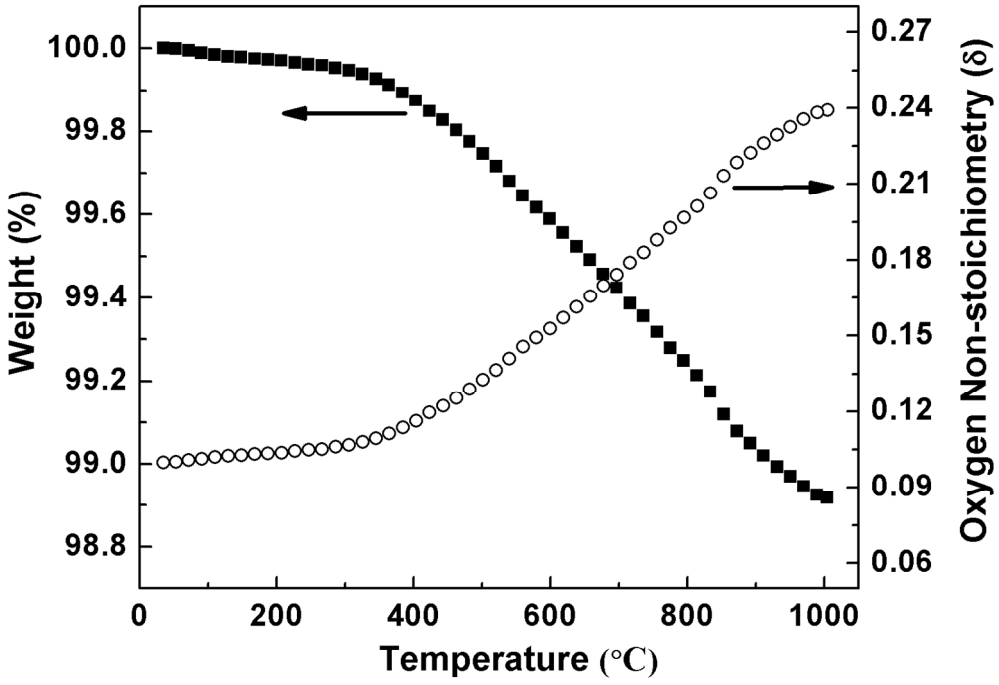

141x97mm (300 x 300 DPI)

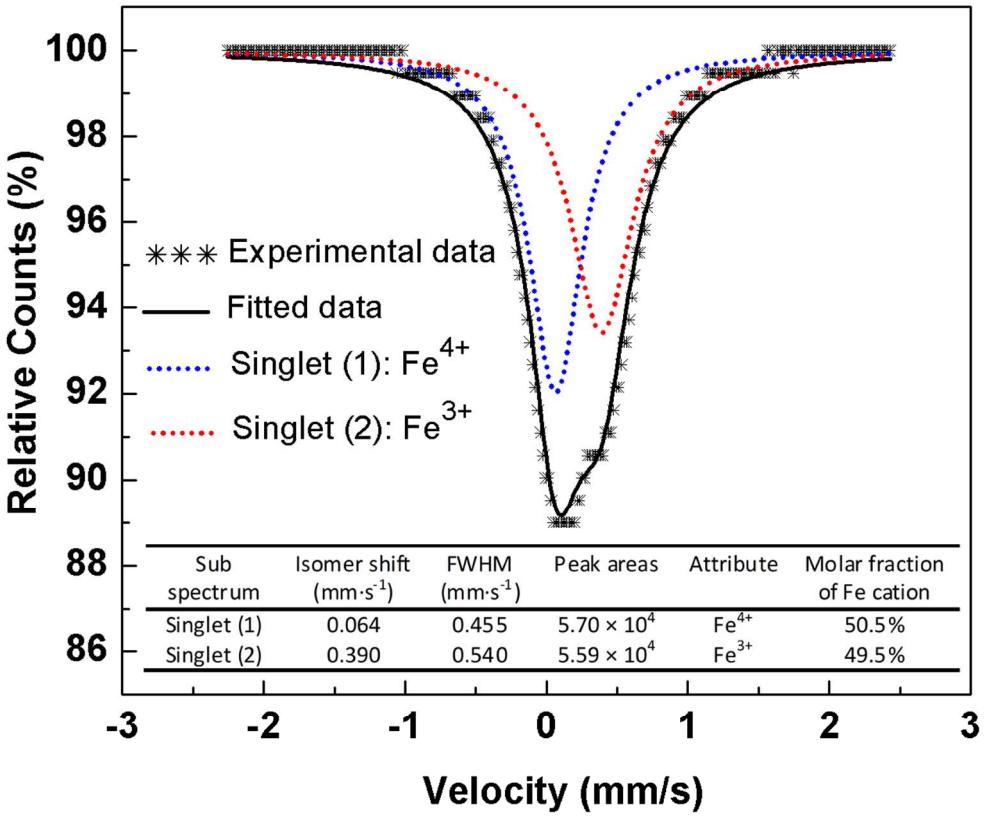

Sub spectrum	Isomer shift ($mm \cdot s^{-1}$)	FWHM ($mm \cdot s^{-1}$)	Peak areas	Attribute	Molar fraction of Fe cation
Singlet (1)	0.064	0.455	5.70×10^4	Fe^{4+}	50.5%
Singlet (2)	0.390	0.540	5.59×10^4	Fe^{3+}	49.5%

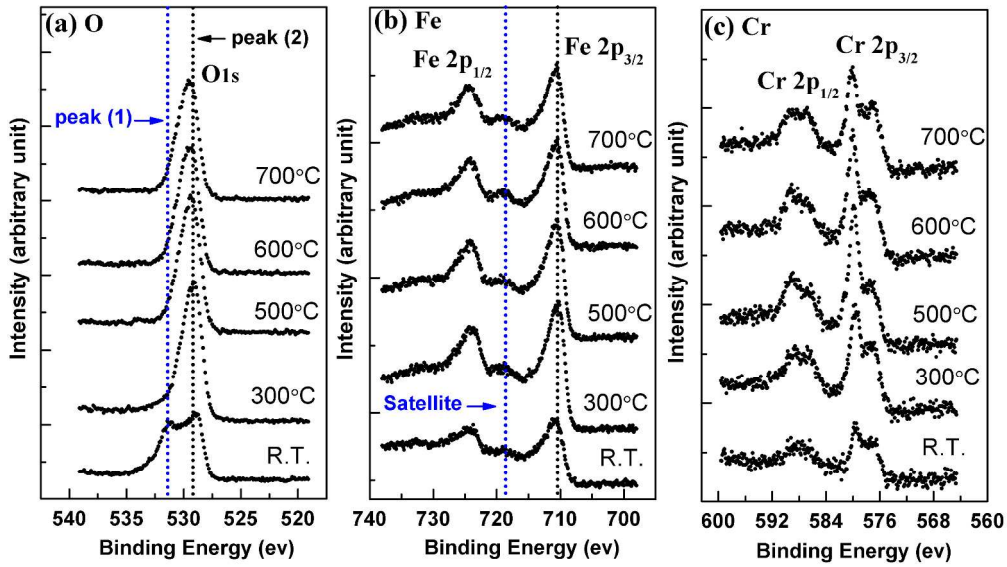

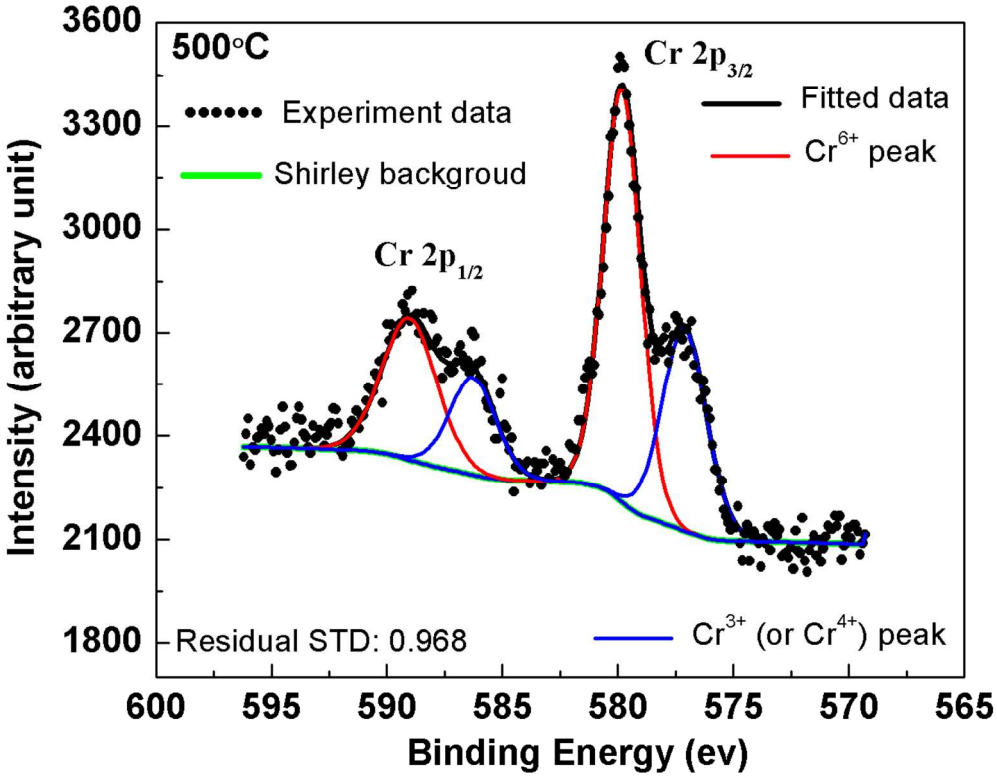

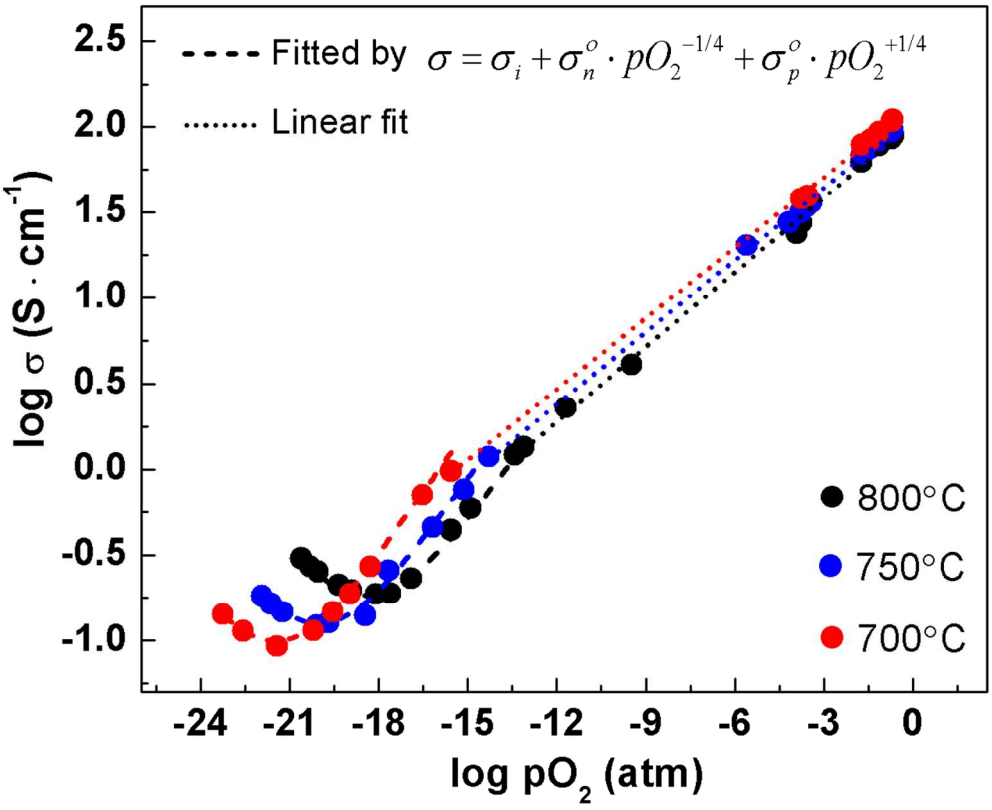

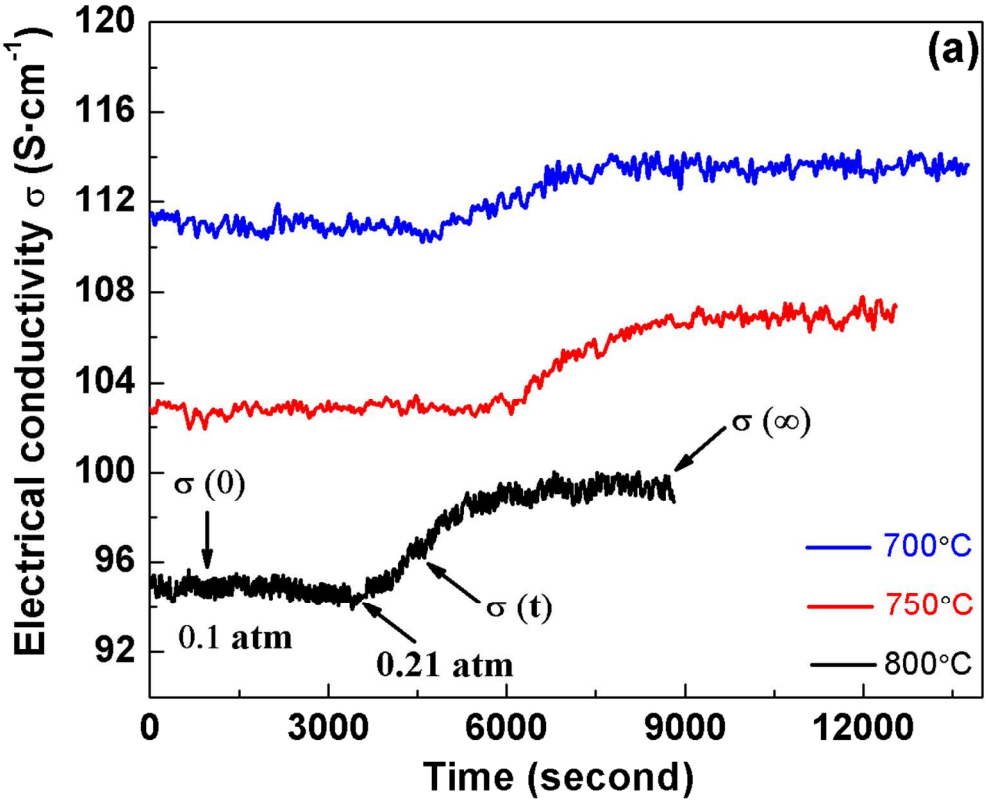

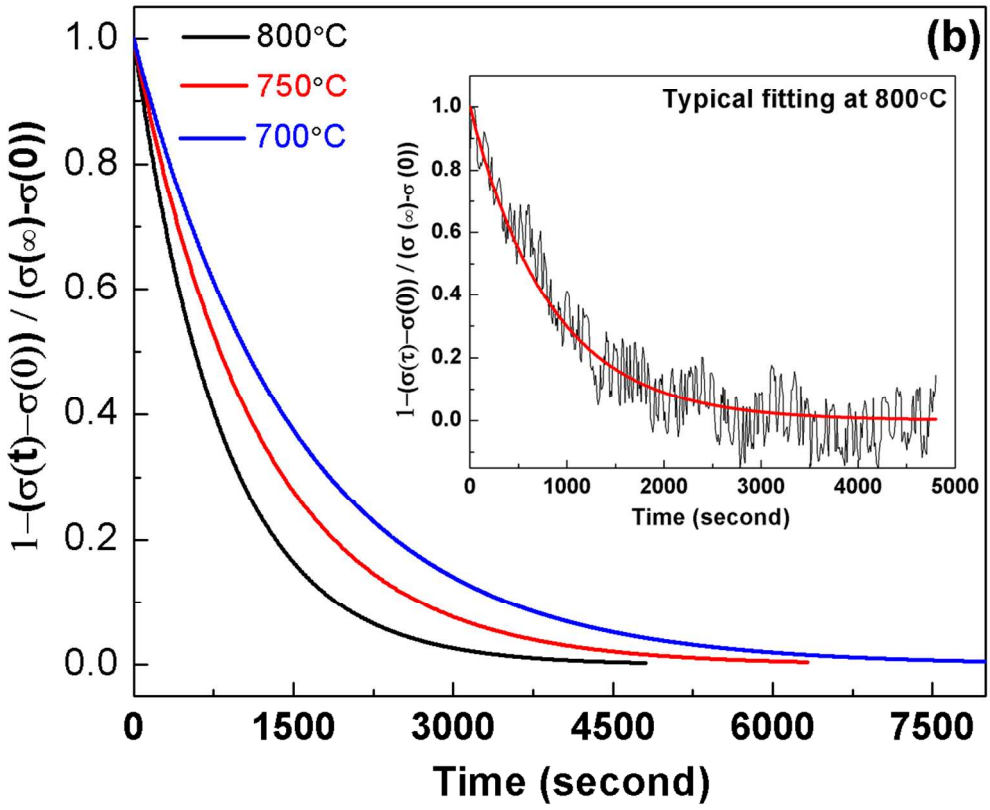

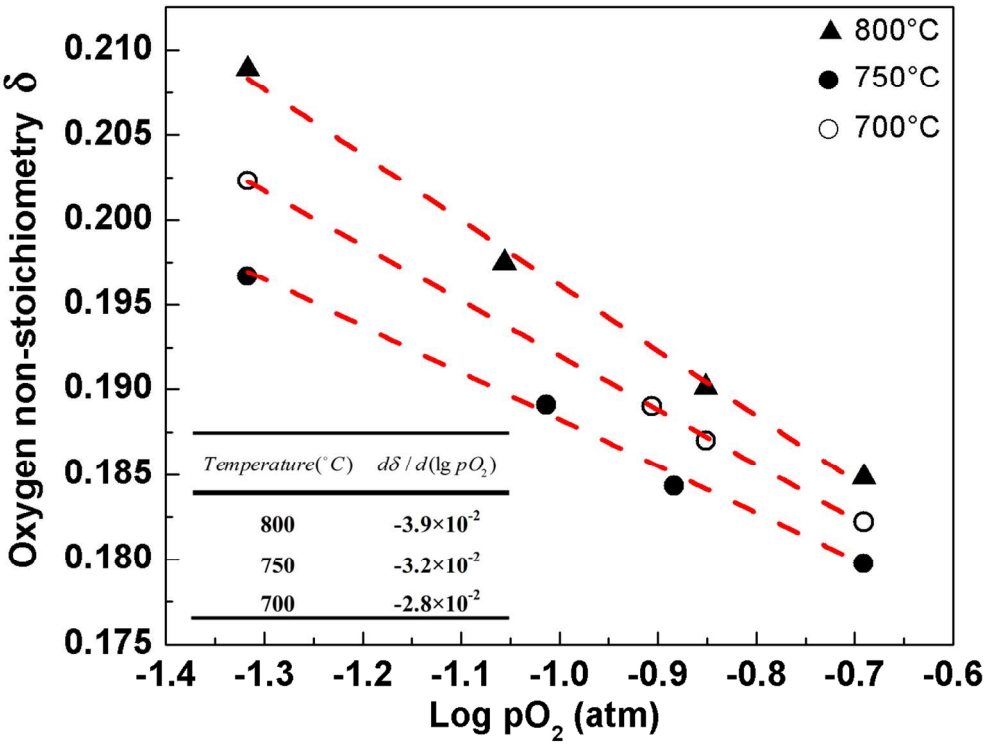

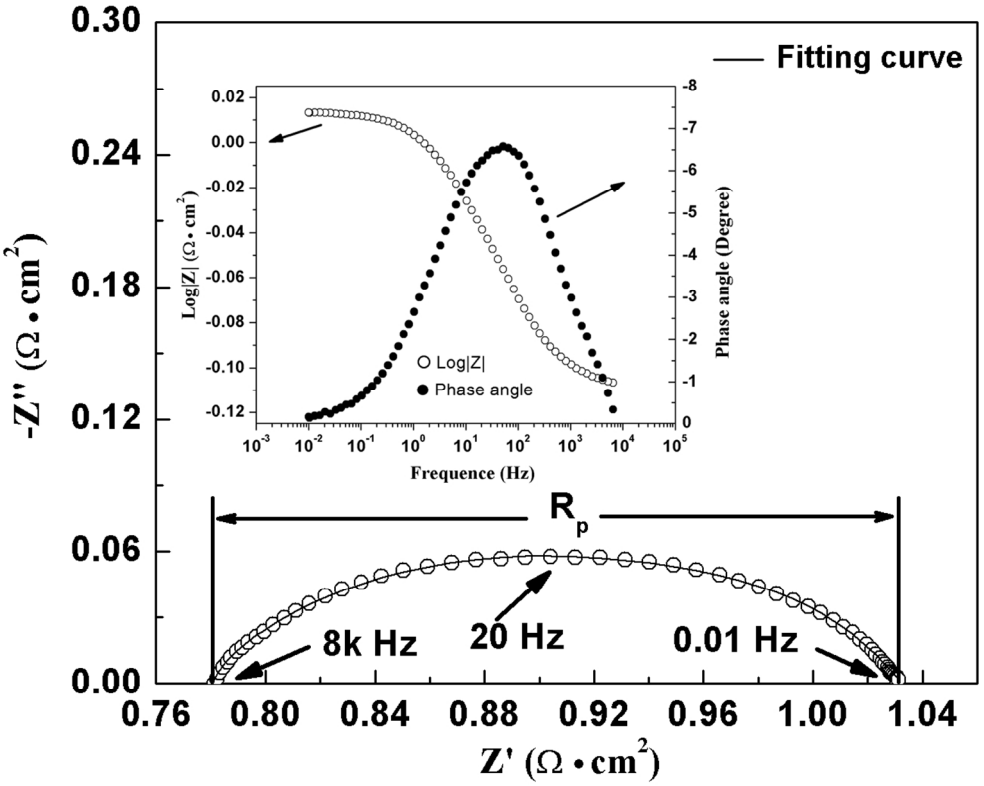

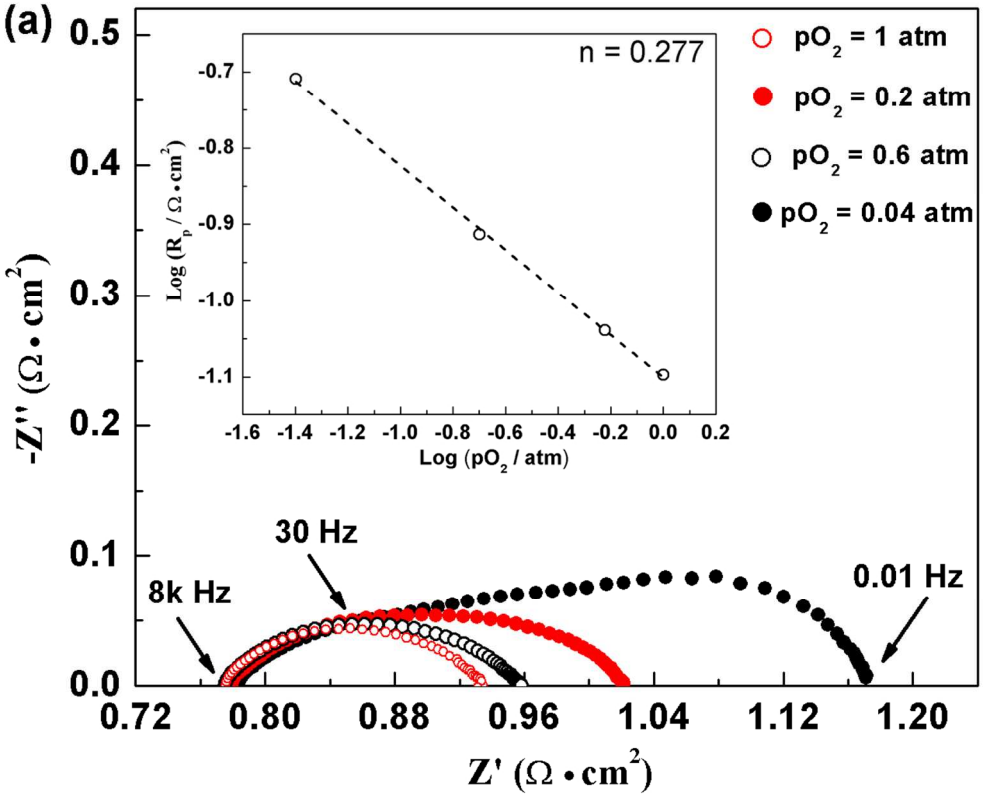

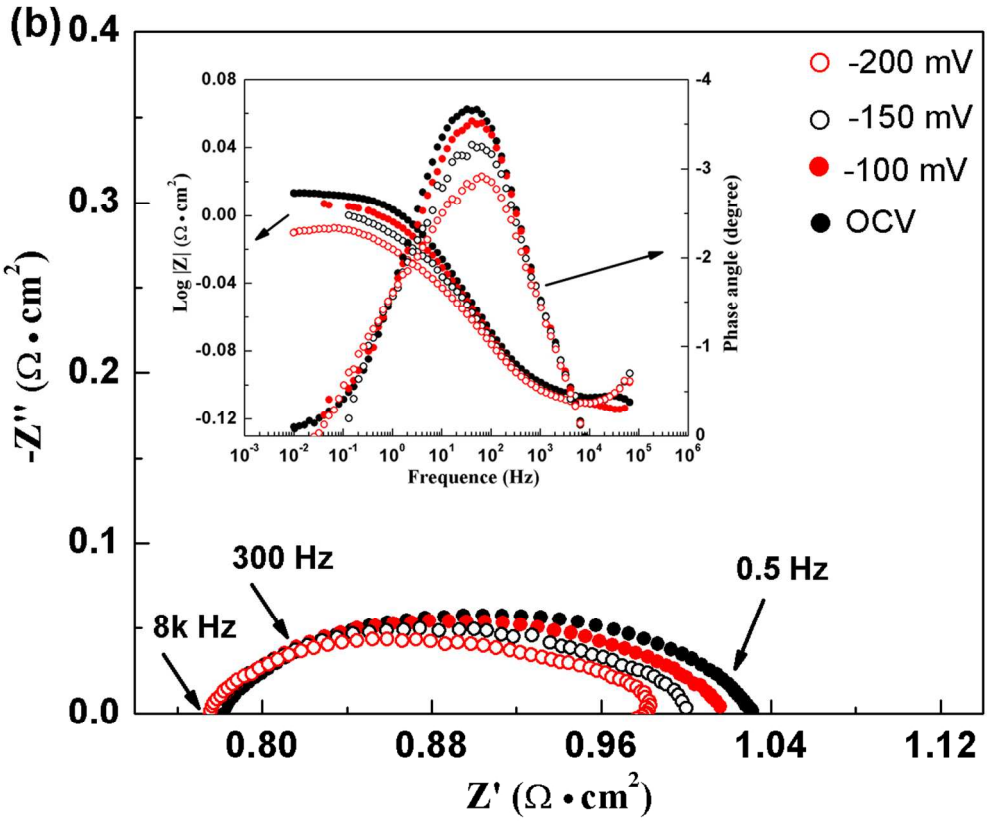

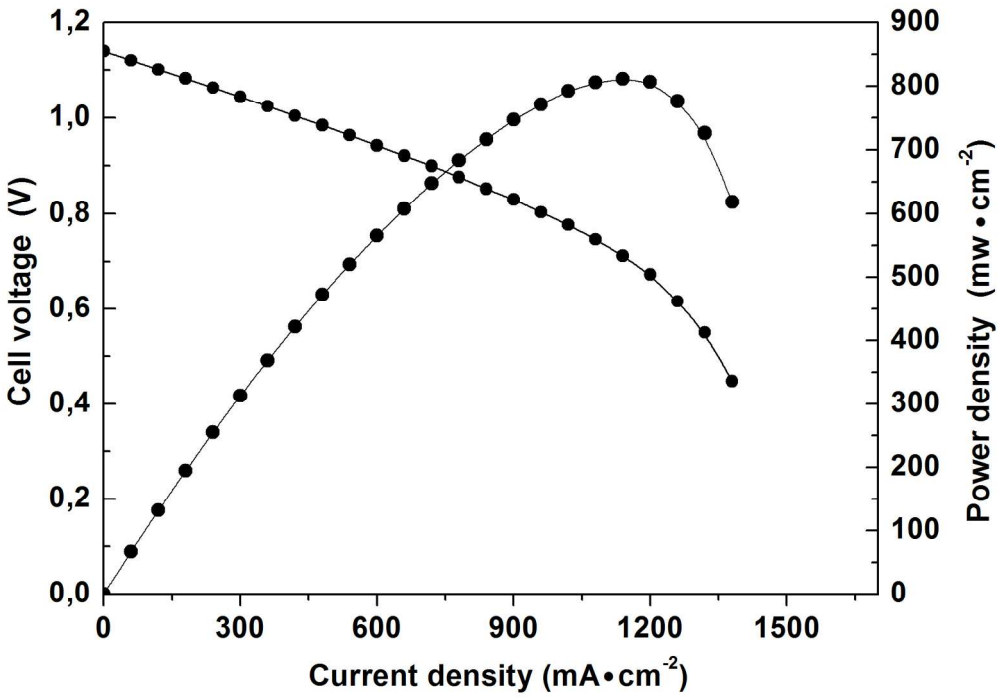

167x116mm (300 x 300 DPI)

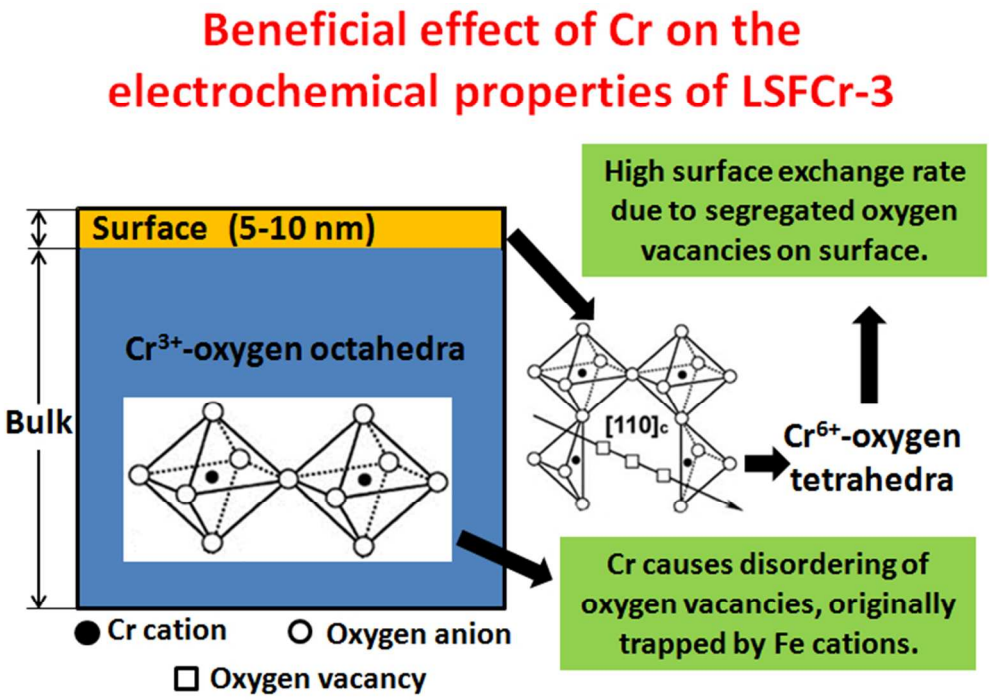

61x43mm (300 x 300 DPI)